Analysis of electron heat transport with off-axis modulated ECRH in Tore Supra

2012 Nucl. Fusion 52 033006

(http://iopscience.iop.org/0029-5515/52/3/033006)

IOP Publishing and International Atomic Energy Agency Nuclear Fusion
Nucl. Fusion **52** (2012) 033006 (16pp) doi:10.1088/0029-5515/52/3/033006

Analysis of electron heat transport with off-axis modulated ECRH in Tore Supra

S.D. Song[1], X.L. Zou[1], G. Giruzzi[1], W.W. Xiao[2], X.T. Ding[2], B.J. Ding[3], J.L. Ségui[1], D. Elbèze[1], F. Clairet[1], C. Fenzi[1], T. Aniel[1], J.F. Artaud[1], V. Basiuk[1], F. Bouquey[1], R. Magne[1], E. Corbel[1] and the Tore Supra Team

[1] CEA, IRFM, F-13108 Saint-Paul-lez-Durance, France
[2] Southwestern Institute of Physics, PO Box 432, Chengdu, People's Republic of China
[3] Institute of Plasma Physics, Chinese Academy of Sciences, Hefei 230031, People's Republic of China

E-mail: gerardo.giruzzi@cea.fr

Received 22 April 2011, accepted for publication 10 February 2012
Published 2 March 2012
Online at stacks.iop.org/NF/52/033006

Abstract
Experiments to study inward heat transport phenomena have been performed in the Tore Supra tokamak with off-axis electron cyclotron resonance heating (ECRH). Both power balance and perturbation transport analysis have been done for low-frequency (1 Hz) ECRH modulation experiments. Heat diffusivity and heat pinch have been separately determined by fitting the experimental data of the amplitude and phase of the Fourier transform of the modulated temperature with a linear transport model including convection term. Comparison with the critical gradient model has shown that the heat pinch previously obtained could include a pseudo-pinch due to the non-linearity of the diffusivity and an additional non-diffusive heat pinch. The pinch effect is reduced for higher densities.

(Some figures may appear in colour only in the online journal)

1. Introduction

The heat transport is one of the fundamental subjects in magnetic confined plasma studies. Inward heat transport is thought to be favourable for the improvement of plasma energy confinement, and it has been observed in some tokamak experiments [1, 2]. In the interpretation of these experiments, some controversies remain. One of them is whether the inward heat flux is purely diffusive or partly convective. By definition, the diffusive heat flux is proportional to the temperature gradient, while the convective part is proportional to the temperature itself. For the convective part, the word 'pinch' is used here to denote the inward convection. Naturally the heat flux q should be a combination of the two terms, which basically can be written as follows:

$$q = -(n\chi\nabla T + nVT) \tag{1}$$

where n is the plasma density, T the (ion or electron) temperature, χ the heat diffusivity and V is the convection velocity. Which part plays a role in the observed inward heat transport is the key point in the debate. In [1, 3], strong off-axis electron cyclotron resonance heating (ECRH) in which 80% of the total energy is deposited outside of $\rho = 0.5$ (ρ is the normalized radius of magnetic surfaces) produced a peaked electron temperature profile, and the power balance analysis, under purely diffusive assumption, yielded a negative diffusivity inside $\rho = 0.5$, which indicates the existence of a heat pinch. In the experiments in RTP [2, 4], FFT analysis for ECRH experiments with modulation frequency of 310 Hz and duty cycle of about 85% produced peculiar fundamental harmonic amplitude profiles, in which the peak is shifted inwards compared with the minimum phase delay, a feature that is different from the usual 'diffusive' behaviour. In the ECRH modulation experiments in ASDEX Upgrade [5], evidence of the combined effect of a critical gradient regulated electron transport and an electron heat pinch term was given. Note that any radial dependence of the heat diffusivity would give a term in the transport equation that is mathematically equivalent to a convection term. In particular, the widely documented critical gradient model (CGM), which includes a strong dependence of diffusivity on the temperature [6], naturally yields a pseudo-pinch, affecting the modulation amplitude.

With the purpose of gaining further knowledge of the inward heat transport, dedicated ECRH modulation experiments have been recently done on Tore Supra. Under low-density conditions, features corresponding to inward heat transport are observed with off-axis ECRH. Modulations are

carried out in order to provide the perturbation transport coefficients and hence FFT analysis is used. In these experiments, a low-modulation frequency (as low as 1 Hz) is chosen, which has not yet been done previously, in order to acquire more harmonics, which is particularly useful for studies of inward heat transport phenomena. In fact, a different behaviour of lower and higher harmonics is known to be a distinctive feature of heat convection.

The paper is organized as follows. Section 2 describes the experimental setup. Experimental results are presented in section 3. In section 4, the results of simulations using a linear pinch model (LPM), based on the analytical solution of a simplified thermal transport equation, are shown. Simulations using the CGM are addressed in section 5. The conclusions are drawn in section 6.

2. Experimental setup

ECRH is an ideal experimental tool for the investigation of electron heat transport, since it has the merits of highly controllable, localized heating profile, simple wave–plasma interaction regime with quasi-optic propagation and direct electron heating. The Tore Supra ECRH system [7] consists of two gyrotrons each capable of injecting ∼300 kW into the plasma, with a deposition width as low as 3 cm. The ECRH system works at the frequency of 118 GHz, i.e. at the fundamental harmonic of the electron cyclotron frequency for the nominal Tore Supra magnetic field (3.8 T). The power is injected in the O-mode polarization from the low-field side, and perpendicularly to the magnetic field for this specific experiment. The ECRH modulation experiments have been carried out in plasmas with major radius $R = 2.43$ m and minor radius of $a = 0.72$ m, current varying from 0.6 to 1 MA, magnetic field on axis 3.73 and 3.53 T, corresponding to deposition positions of $\rho = 0.5$ and 0.6, line-averaged density (1.4–5.4) $\times 10^{19}$ m^3, central electron temperature 2–5 keV. With the conditions above, good first-pass power absorption is obtained in all the cases considered. The EC wave absorption has been computed with the help of the fully relativistic ray-tracing code REMA [8], using the global experimental parameters of the discharge (major and minor radius, magnetic equilibrium) and the measured electron density and temperature profiles. The total fraction of absorbed power is found to be 93% for discharge 40504 and 86% for discharge 43234. In the worse case (43234), the 14% of the power that is not absorbed is reflected on the wall, possibly changing polarization, poloidal and toroidal angles. After calculation, it is found that the variation of the toroidal angle leads to a broadened power absorption, whereas variation of the poloidal angles leads to further off-axis power absorption. The reflected power absorbed inside $\rho = 0.5$, where the study of the heat pinch is of importance, is typically at least a factor >50 lower than the incident absorbed power, therefore always negligible. For $\rho < 0.3$, the EC power cannot be absorbed at all, for lack of appropriate resonance conditions. Moreover, note that if the amplitude growth were due to spurious ECRH central power it would not vanish at high frequency and it would lower the central phase values, which is clearly not the case in the experimental observation. We can therefore rule out this type of effect.

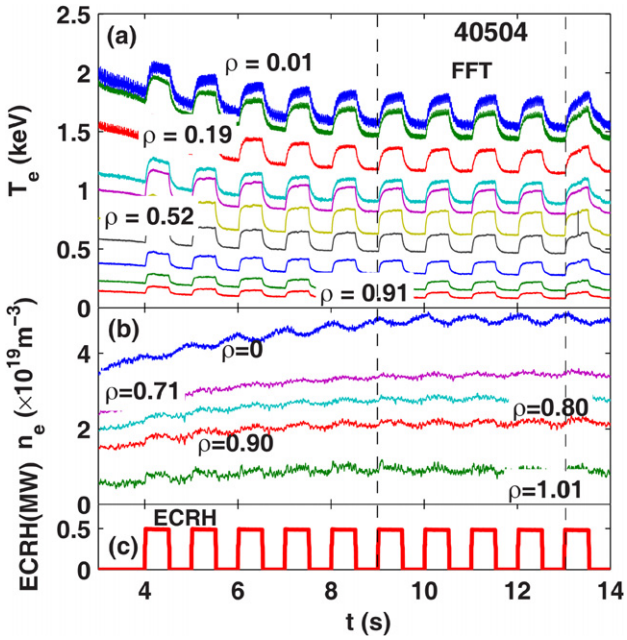

Figure 1. Temporal evolution of (*a*) the electron temperature (ECE), (*b*) density (reflectometry) and (*c*) the ECRH power (TS#40504). The density in (*b*) at $\rho = 0$ is taken from the interferometry. The FFT time window is shown between the two dashed lines.

Square wave modulations have been performed with a duty cycle of 50%. In previous ECRH modulation experiments in other tokamaks, the modulation frequency range is from 30 to 300 Hz. In our experiments the modulation frequency is chosen to be as low as 1 Hz. The advantages of using a low-frequency modulation in the perturbation transport analysis are (1) a large perturbation amplitude with high signal-to-noise ratio; (2) having many harmonics (first to eleventh); (3) to be less affected by sawteeth and other perturbations; (4) the most important is to be more sensitive to the convection (heat pinch) effect. Indeed the higher the modulation frequency, the smaller the convection effect compared with the diffusion effect. Of course there are also disadvantages for the low-frequency modulation: (1) the transport coefficients varying along with the heat pulse; (2) more requirements for plasma control; (3) an additional parameter should be taken into account with the damping time which characterizes the loss term (see discussion in section 4.2); (4) the influence of the edge boundary condition on the propagation characteristics of the perturbation and in the modelling should also be taken into consideration; (5) at a very low-modulation frequency, the FFT results might be influenced by the slow evolution of the parameters, the choice of the time interval is therefore important.

The electron temperature profile was measured by a 32-channel heterodyne ECE radiometer, with a spatial resolution of about 2.5 cm [9]. The cross-calibration precision between channels is better than 3%, which allows high-quality temperature profile measurements. The time resolution is 1 ms for our experiments. The ion temperature was measured by charge-exchange recombination spectroscopy [10]. The density profile is measured by two sets of X mode heterodyne reflectometers, working at frequencies ranging from 50 to 110 GHz and from 105 to 155 GHz, respectively. The

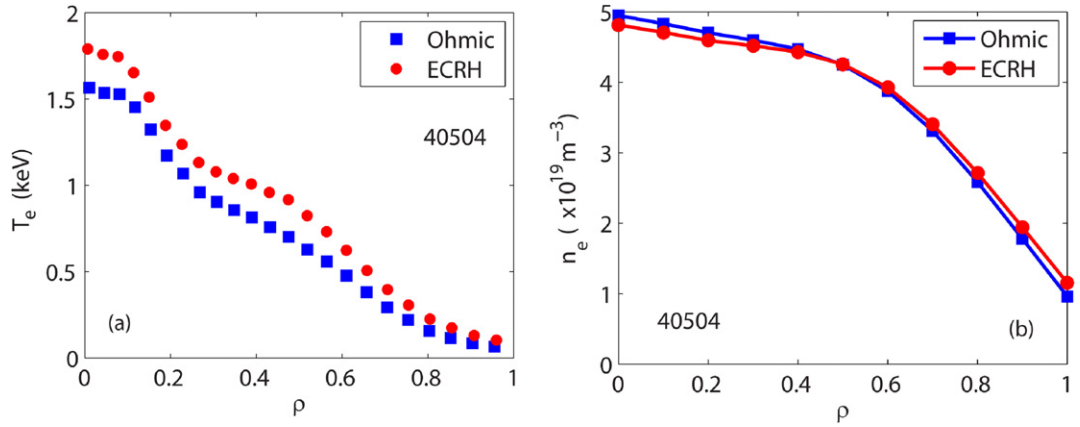

Figure 2. Electron temperature (ECE channels) (*a*) and density (Abel-inverted interferometry data) (*b*) profiles for shot 40504. The ohmic phase corresponds to $t = 9.9$ s, and the ECRH phase corresponds to $t = 10.4$ s.

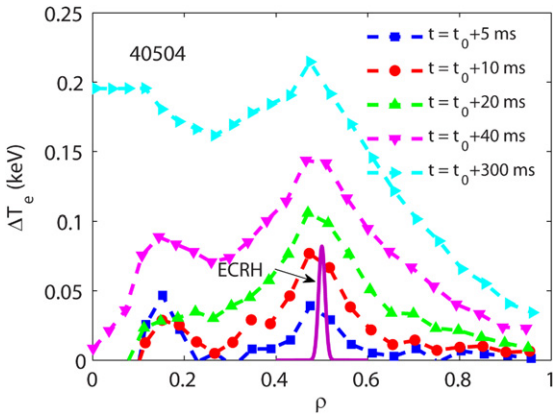

Figure 3. Time evolution of the electron temperature perturbation profile during an ECRH modulation pulse for shot TS#40504 ($t_0 = 10.02$ s).

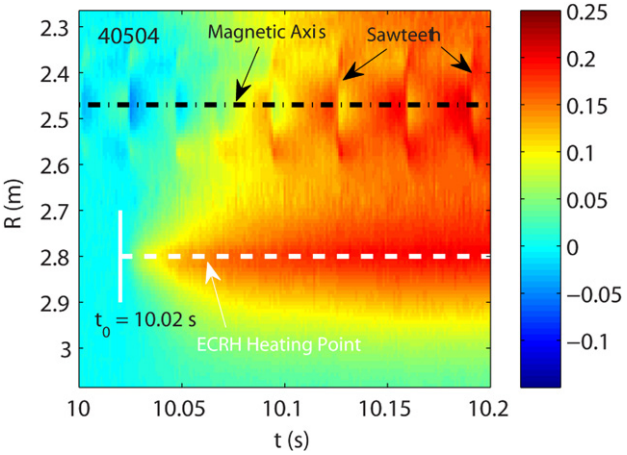

Figure 4. 2D temporal–spatial image of the T_e perturbation during ECRH for shot TS#40504.

frequency sweeping time is up to 20 μs, and the profile uncertainty is less than 1 cm [11, 12]. A 9 channel infrared interferometer, which has a spatial resolution of ~7 cm, is also used for the measurement of density profile in case the reflectometers cannot cover the whole range of plasma radii [10].

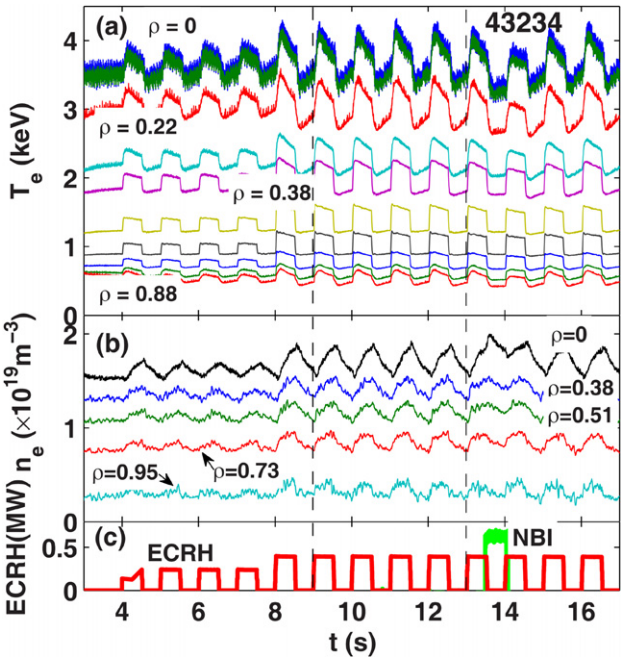

Figure 5. Temporal evolution of (*a*) the electron temperature (ECE), (*b*) the electron density (reflectometry) and (*c*) ECRH power. The injection of neutral beam (NBI) is also shown in (*c*). (shot TS#43234).

3. Experimental results

Different transport behaviours have been observed for two densities: a high-density regime with central density $n_{e0} = (3\text{–}5) \times 10^{19}\,\mathrm{m}^{-3}$, and a low-density regime with $n_{e0} = (1\text{–}2) \times 10^{19}\,\mathrm{m}^{-3}$. These two cases are illustrated in the next two sub-sections.

3.1. High density

Figure 1 presents the time evolution of the electron temperature and density, for a deuterium discharge in which the ECRH power was deposited at $\rho_{dep} = 0.5$ on the equatorial plane. The main plasma parameters are the following: magnetic field $B_T = 3.73$ T, plasma current $I_p = 700$ kA, central density

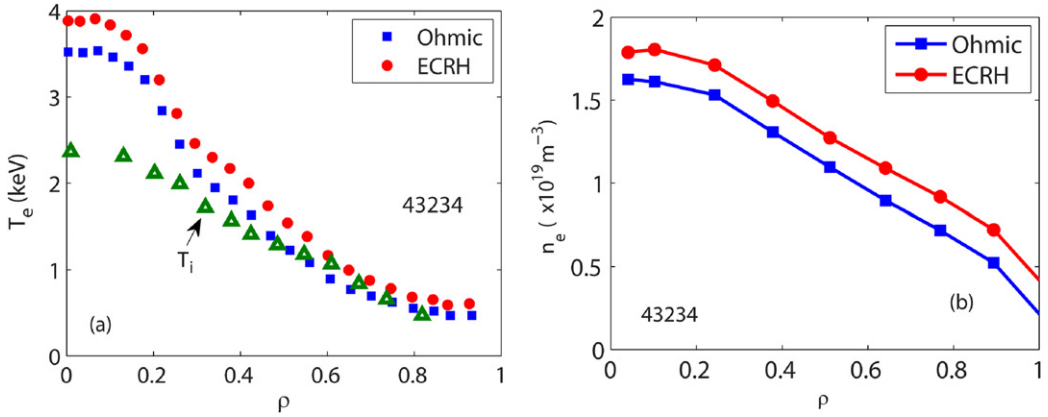

Figure 6. The electron temperature (ECE) (*a*) and density (reflectometry) (*b*) profiles for shot 43234. Ohmic phase corresponds to $t = 9.9$ s; ECRH phase corresponds to $t = 10.4$ s. The measured T_i profile at $t = 13.9$ s is also presented in (*a*).

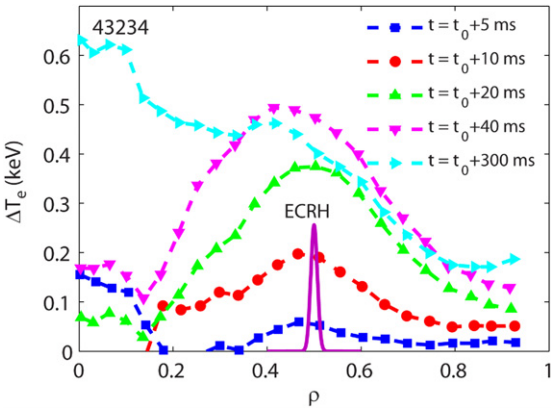

Figure 7. The perturbed electron temperature profiles (ECE) at various times during an ECRH pulse. T_e profile at $t_0 = 11.015$ s is selected as the reference profile.

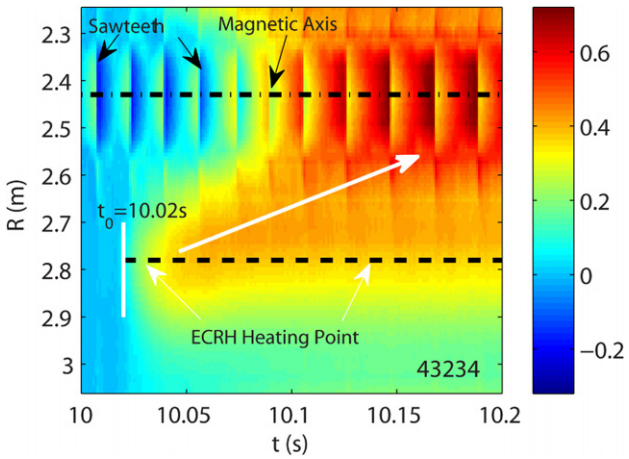

Figure 8. 2D temporal–spatial image of the electron temperature perturbation (ECE) for shot TS#43234.

$n_{e0} = (4\text{–}5.4) \times 10^{19}\,\mathrm{m}^{-3}$, edge safety factor $q_{edge} = 6.3$. Other discharges with high density (i.e. roughly (3–5) $\times$ $10^{19}\,\mathrm{m}^{-3}$) and half-radius ECRH deposition display similar effects. The ECRH modulation is carried out at a frequency of 1 Hz with 100% amplitude rise and fall, square waveform and duty cycle factor of 50%. The ECRH power (~600 kW) is applied between 4 s and 14 s. During the time interval from 4 s to 8 s the density increases, while the temperature decreases. For the time interval from 8 s to 14 s, the perturbation of T_e is ~10% of the average T_e, which remains reasonable for a perturbation analysis. In this case, it should be noted that the density is moderately modulated by ECRH. Figure 2 shows the T_e and n_e profiles at $t = 9.9$ s (ohmic phase) and $t = 10.4$ s (ECRH phase).

Figure 3 shows the T_e incremental variation profile during one ECRH pulse. The ΔT_e is defined as the difference between the electron temperature in the ECRH phase and in the ohmic phase, where the T_e in the ohmic phase is taken from $t_0 = 10.02$ s, which corresponds to a time just before the injection of ECRH power. The time $t = t_0 + 300$ ms corresponds to the 'saturation' phase of the ECRH regime. From this figure, we can observe that during the ECRH phase the heat starts to increase from the ECRH deposition layer, and then spreads inside and outside of this layer due to transport processes. Here the maximum of the temperature perturbation remains unchanged at the ECRH deposition. This indicates that in this case the dominating transport process is the diffusion, while the heat convection, if it exists, should be small. A secondary local maximum of the temperature perturbation is located at $\rho = 0.15$ just outside the $q = 1$ surface, where the sawteeth inversion radius locates between $\rho = 0.08$ and $\rho = 0.11$. As the region inside the $q = 1$ surface is affected by sawtooth activity, it is also possible that the secondary local maximum is not due to a transport process.

A useful representation of the heat transport process is the time-space evolution of the temperature perturbation, which is shown in figure 4. The heating position corresponds to the starting point of the temperature perturbation, which is located around $R = 2.8$ m or $\rho = 0.5$. In this case, the most heated part remains peaked at the predicted maximum of the EC wave absorption, which means that the diffusion effect is dominant.

3.2. Low density

Experiments with ECRH performed in low-density plasmas (i.e. $n_{e0} = (1\text{–}2) \times 10^{19}\,\mathrm{m}^{-3}$) show different behaviours for the temperature perturbation with respect to the high-density ones. Figure 5 shows the time evolution of electron temperature and density for shot TS#43234. In this shot,

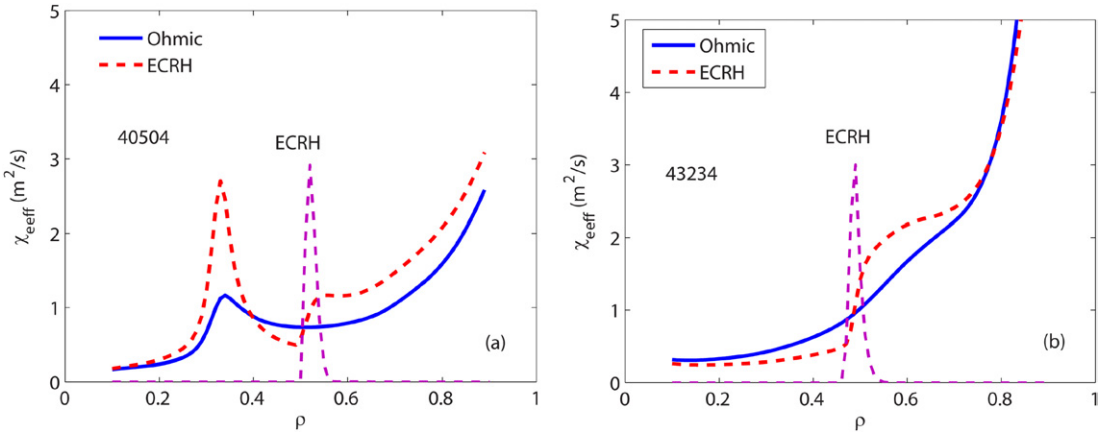

Figure 9. Heat diffusivity χ_{eff} from power balance analysis with CRONOS. (*a*) is for shot 40504 and (*b*) is for shot 43234.

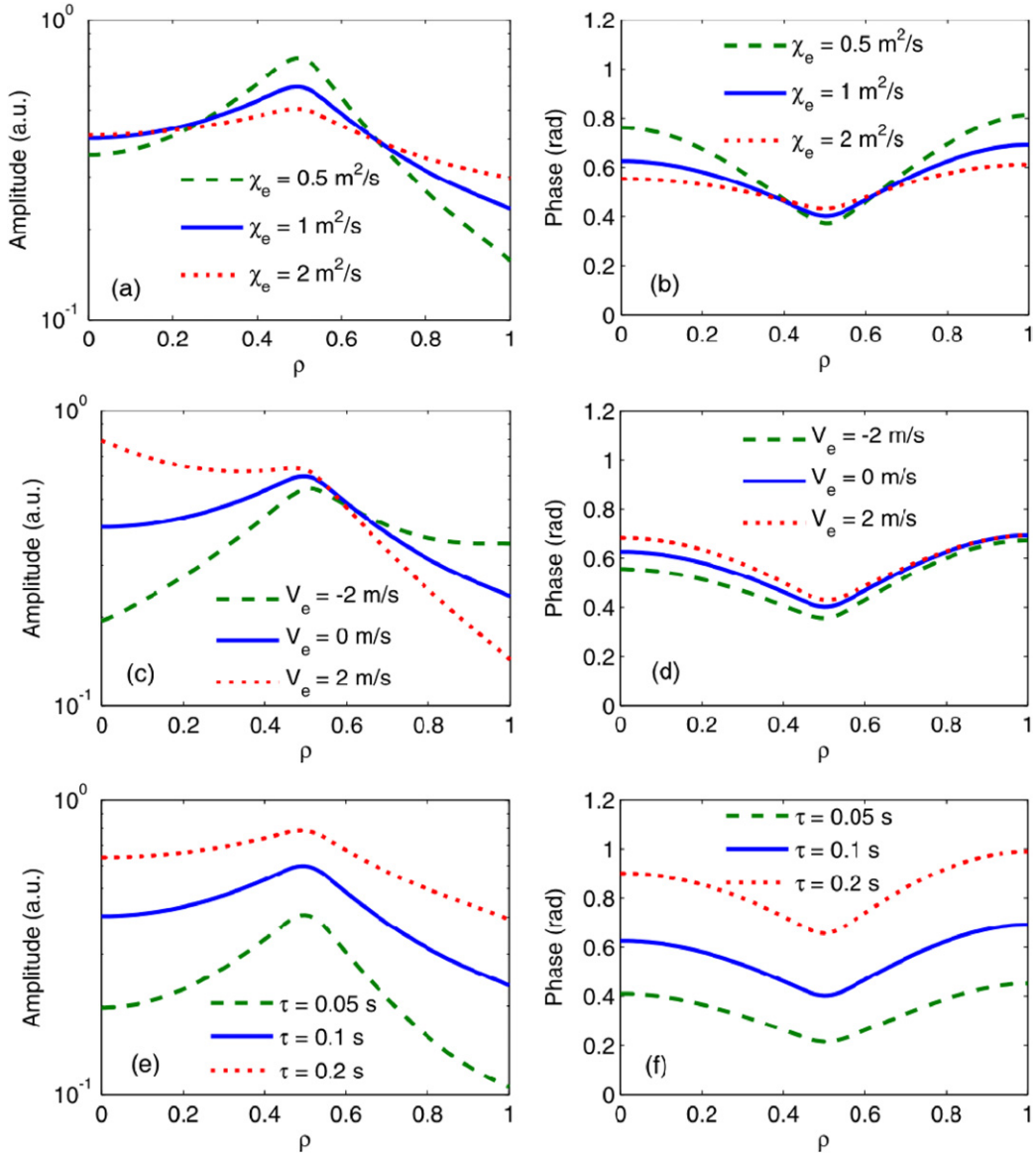

Figure 10. Influence of electron diffusivity χ_e, convection velocity V_e (here positive value means inward) and damping time τ on the amplitude and phase profiles of $\tilde{T}_e$. (*a*) and (*b*) show the influence of χ_e; (*c*) and (*d*) that of V_e; (*e*) and (*f*) that of τ. The solid lines correspond to the same transport coefficients.

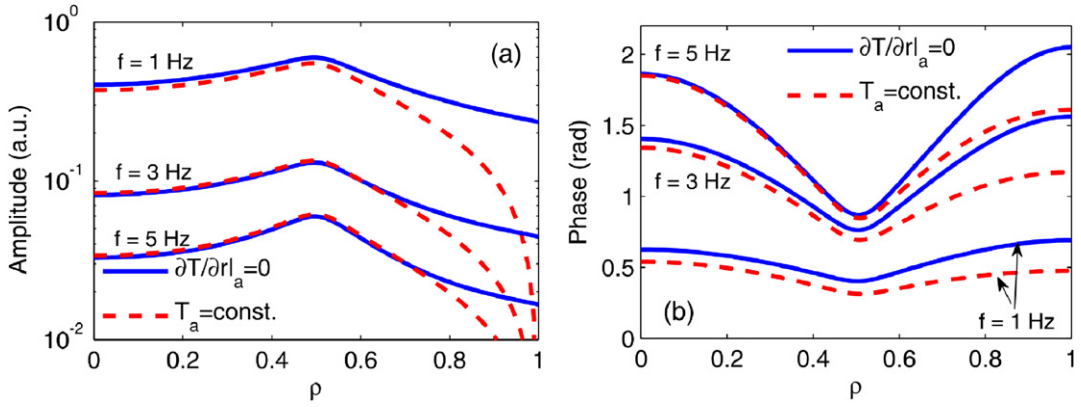

Figure 11. Influence of boundary conditions on the amplitude (*a*) and phase (*b*) profiles for the first three harmonics ($\chi_e = 1\,m^2\,s^{-1}$, $V_e = 0\,m\,s^{-1}$ and $\tau = 0.1\,s$).

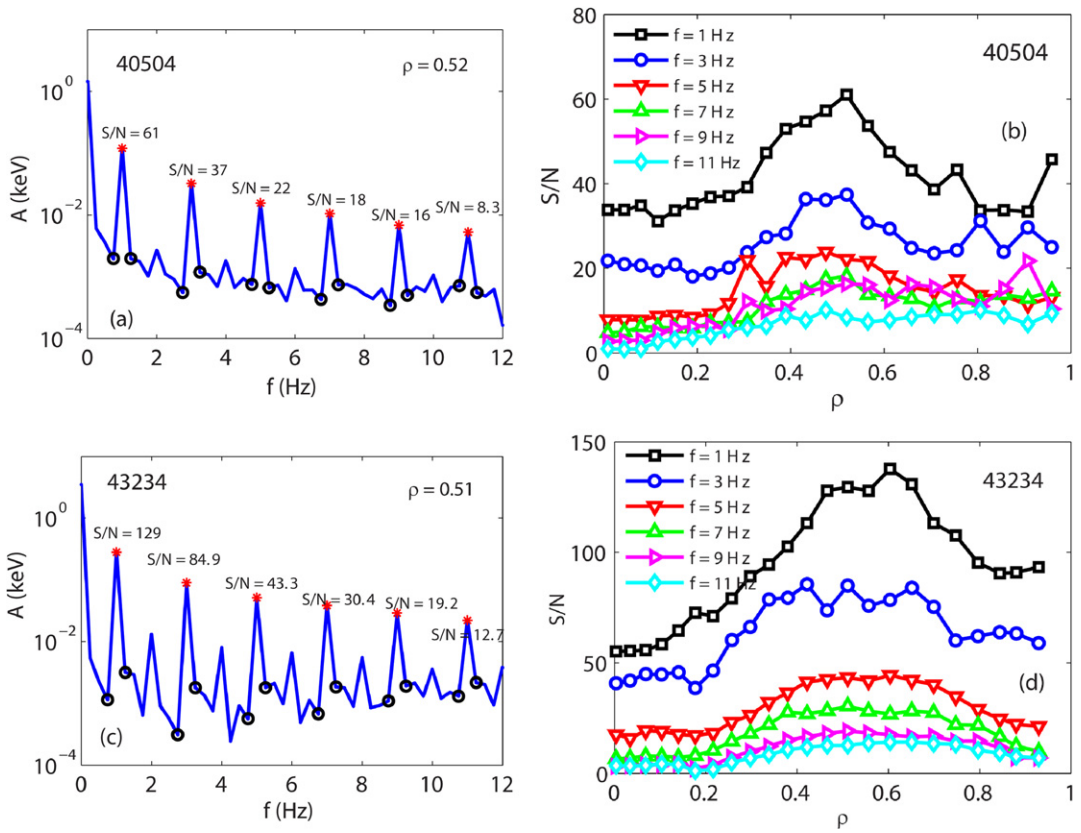

Figure 12. Signal-to-noise ratio (SNR) of the harmonics of T_e in the time interval (9–13 s). SNR around the ECRH heating position for TS#40504 (*a*) and TS#43234 (*c*). SNR profiles of harmonics from the first to the eleventh for TS#40504 (*b*) and TS#43234 (*d*).

the two gyrotrons are switched on subsequently ($t = 4\,s$ for the first gyrotron, then $t = 8\,s$ for the second one), which produces temperature perturbations of different levels. The main parameters for this shot are $B_T = 3.72\,T$, $I_p = 700\,kA$, $n_{e0} = (1.5–1.8) \times 10^{19}\,m^{-3}$, $q_{edge} = 6.6$. The modulation frequency is 1 Hz, and the injected ECRH power is about 300 kW from 4 to 8 s and 600 kW from 8 s to 17 s. At $t = 13.485\,s$, the diagnostic neutral beam is injected into the plasma in order to measure the ion temperature T_i profile by charge-exchange spectroscopy. The power of the neutral beam is ~350 kW, hydrogen is injected at an energy of 50 keV, for 600 ms. Note that measurements of the ion temperature are only available at this time of the discharge, when the beam power is applied. The ion temperature is therefore computed by means of the CRONOS code using the measurement as a constraint and taking into account the perturbation of the density by the neutral beam. In the modulation analysis this simulated ion temperature is used. Owing to the low electron–ion coupling in this low-density discharge, the sensitivity to the exact shape of T_i is limited. This has been checked by a sensitivity analysis.

In this shot, the waveforms of the electron temperature and density perturbation are quite different from shot TS#40504, especially for the central channels. The temperature evolution

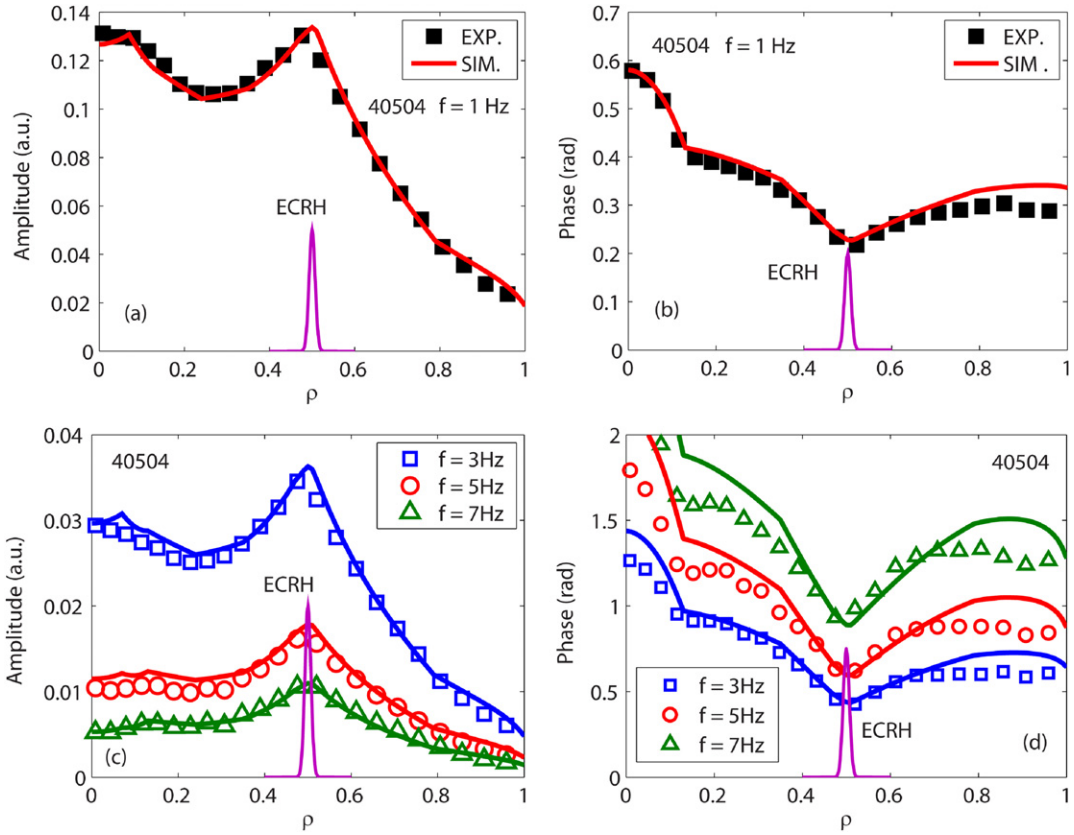

Figure 13. Simulation using the LPM for high density (TS#40504). The discrete points are experimental values, and the solid lines represent the simulation. Amplitude (*a*) and phase (*b*) of the fundamental harmonic. Amplitude (*c*) and phase (*d*) of the third, fifth and seventh harmonics.

in one ECRH modulation period can be divided into four phases as described in the following: a drastic temperature increase for 100 ms, then a slow temperature decrease for 400 ms, when ECRH is switched on; a drastic temperature decrease for 100 ms, then a slow temperature increase for 400 ms, when ECRH is switched off. For this discharge the electron density is as low as the natural density of the vacuum vessel, i.e. without gas injection. From 4 to 8 s, the density perturbation level at $\rho = 0.5$ is 3% of its mean value, while the temperature perturbation level at the same position is 7%. From 8 to 13 s, the density perturbation level is 6%, while the temperature perturbation level is 12%. It should be noted that at low density, the density is modulated in phase with the ECRH power (i.e. it increases during the power pulse), while at high density, outside $\rho = 0.75$ the density is modulated in phase while inside $\rho = 0.75$ it is in opposition of phase (i.e. it decreases when the EC power is applied.)

Figure 6 shows the T_e and n_e profiles measured at $t = 9.9$ s (ohmic phase) and $t = 10.4$ s (ECRH phase) for shot TS#43234, the ion temperature T_i measured at $t = 13.9$ s is also shown. The electron temperature profile measured by ECE outside $\rho \sim 0.6$ is relatively high compared with shot TS#40504, since the optical depth for the EC wave is less than 2 there. The ECE data in this part include wall reflection effects, leading to an overestimation of the electron temperature. However, it is difficult to quantify the overestimation of the electron temperature in regions of low-optical depth and low density, because in the same region the measurements of Thomson scattering are also affected by a significant error. Comparison with Thomson scattering data suggests that the overestimation increases with minor radius, from ~10% at $\rho = 0.6$ to 20–30% at $\rho = 0.7$ up to >50% at $\rho > 0.8$.

Figure 7 shows the electron temperature profile evolution during ECRH. The temperature perturbation profile is broader compared with that of the high-density case (TS#40504), and manifestly asymmetric from 10 ms after ECRH is turned on, i.e. the temperature increment inside the ECRH power deposition layer is relatively larger. It should be noted that the maximum of the temperature perturbation at $t = 300$ ms is now shifted towards the centre. The little secondary maximum inside $\rho = 0.2$ (also present on figure 3) is probably due to sawteeth. This effect is more visible in figure 8, which displays the 2D temporal–spatial image of the electron temperature perturbation. Indeed, from this figure we can see that the ECRH driven heat, represented by red, propagates inwards from the ECRH deposition to the centre, as shown in figure 8 by an arrow. This behaviour may be due to either the existence of inward heat pinch or lower diffusivity inside. For the latter there should be a transport barrier, around which a steep diffusivity exists, preventing outward heat transport. In the next sections Fourier analysis and simulation with transport model will be done in order to determine which is the actual mechanism responsible for this observation.

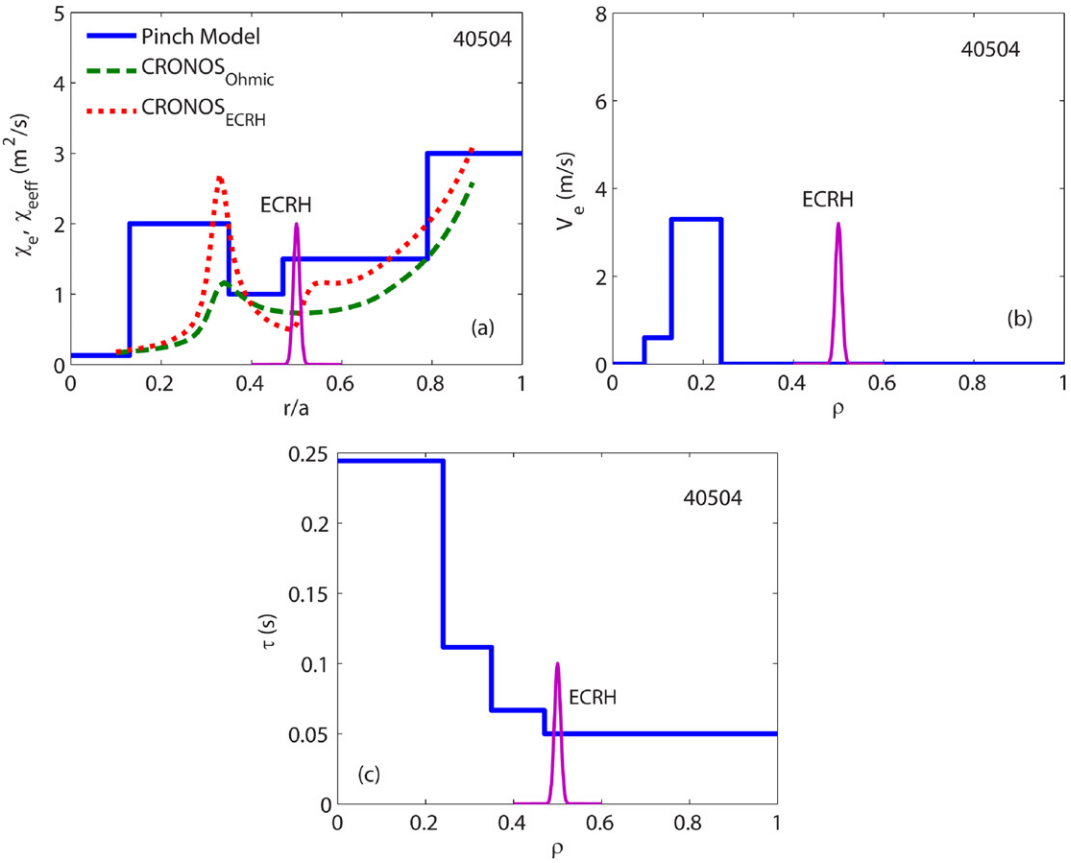

Figure 14. Parameters used for the simulation with the LPM shown in figure 13. (*a*) Diffusivity obtained by the LPM (solid line), by CRONOS in the ECRH regime (dotted line) and in the ohmic regime (dashed line). (*b*) Pinch velocity (positive for inward). (*c*) Damping time.

4. Simulation using the LPM

Transport analysis for both stationary and transient behaviour has been performed for the discharges described in section 3. Since the ohmic and ECRH phases of the modulations last 500 ms and the energy confinement time is of the order of 200 ms, the final times of each phase can be reasonably used for power balance analysis, performed by means of the CRONOS code [13]. For the transient phase or temperature modulation, an analytical solution of the simplified transport equation has been used for the simulation [14]. Finally, the empirical CGM [6] has been used for the simulation of both stationary and transient behaviour.

4.1. Power balance analysis for steady state

The CRONOS code solves coupled diffusion equations (current, heat, particles). The simulation of the above two discharges are performed in the interpretative mode, in which only the current diffusion equation is solved predictively. Using the measured electron density and temperature profiles, heat diffusivity can be determined, in the final 100 ms before the end of each modulation phase. Both the power balance and the FFT analyses have been performed in the last few modulations, where temperature, density and current profiles have almost stopped their slow evolutions ($t > 5$ s). Figure 9 shows the effective transport coefficients assuming pure diffusive transport, (*a*) for shot TS#40504 and (*b*) for shot TS#43234. It appears that ECRH produces a marked change in the profile of the heat diffusivity, around the absorption location: the diffusivity increases outside and decreases just inside the ECRH peak ($0.4 < \rho < 0.5$). This asymmetry or jump in the heat diffusivity in the presence of ECRH around the power deposition could be explained by the existence of a critical temperature gradient [15]. Furthermore, this change in diffusivity profile is much larger for low density than for high density. The global confinement of course decreases in the presence of ECRH. The peak at $\rho \sim 0.3$ in figure 9(*a*) is probably an artefact associated with sawteeth. Note that from this power balance analysis negative diffusivity is not found, therefore inward pinch is not strictly necessary to explain the stationary behaviour. However, it will be shown in the following that inward convection is a good candidate to explain the response to power modulations of low-density discharges of this type.

4.2. LPM and determination of transport coefficients

Usually, the usefulness of the power balance analysis is restricted due to the uncertainty of source profiles and the lack of experimental data for some profiles such as the ion, impurity and radiation. Another disadvantage is the fact that there is no separation between diffusion and convection in this approach. However, perturbation transport analysis can provide additional information, and particularly the separation

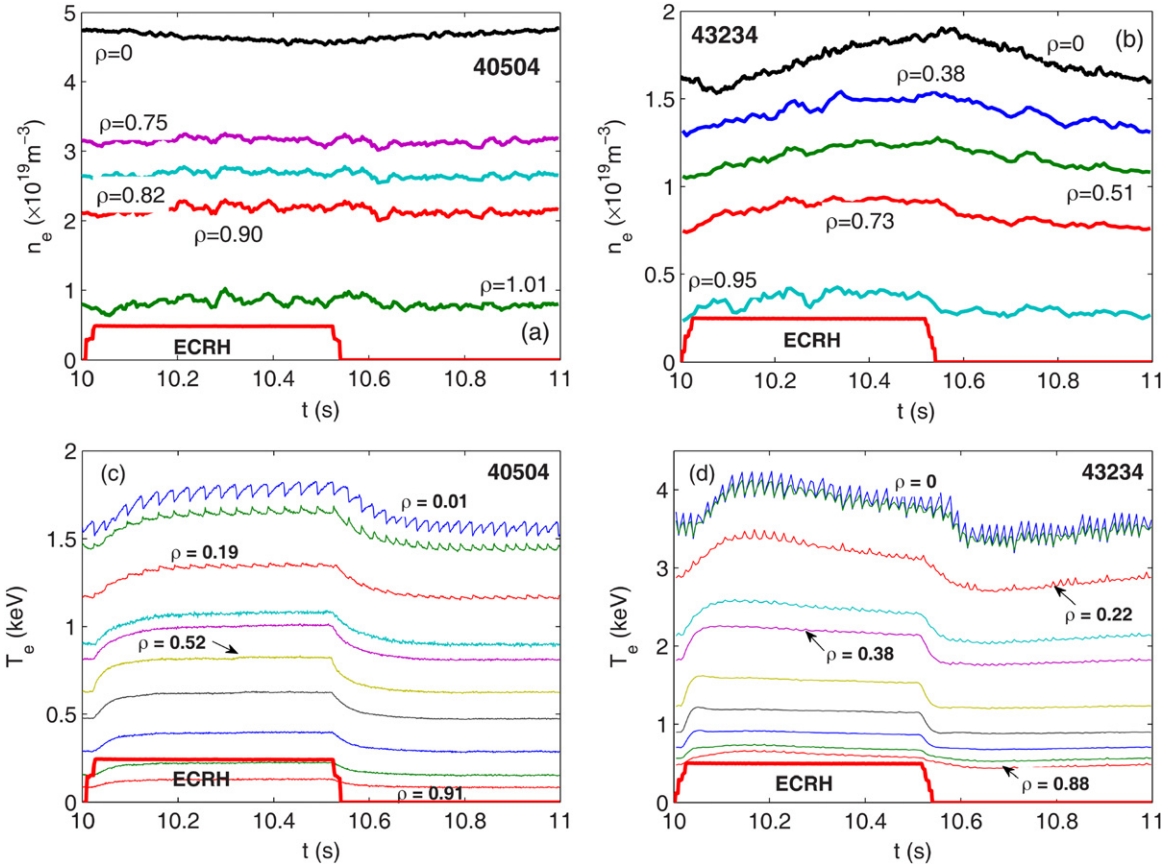

Figure 15. (*a*) and (*b*) are density evolution curves at high- (*a*) and low- (*b*) density cases, respectively, during one ECRH modulation period. (*c*) and (*d*) are analogous curves for the electron temperature

between diffusion and convection becomes possible. Of course the combination of these two methods is often necessary and useful.

In order to treat the problem analytically, a simplified transport model is used and the transport equation for the temperature perturbation $\tilde{T}_e$ is cast in the following form:

$$\frac{3}{2}\frac{\partial n_e \tilde{T}_e}{\partial t} - \nabla \cdot (n_e \chi_e \nabla \tilde{T}_e + n_e V_e \tilde{T}_e) + \frac{3}{2}\frac{n_e \tilde{T}_e}{\tau} = \tilde{S}_h \qquad (2)$$

where τ is the damping time which represents all the heat loss terms, including radiation, energy transfer to the ions, decrease of the ohmic source during ECRH; χ_e and V_e are diffusivity and convection velocity of the electron channel, respectively. Note that here positive V_e means inward transport. Here the values of these three parameters are assumed to be constant in time, by which analytical solution with the Green function method is obtained [14, 16, 17]. The $\tilde{S}_h$ term is the modulated ECRH heating source. Here the coordinate is cylindrical, and the radii are those of circular flux surfaces. This LPM will be used for the following simulation.

In practice, the crucial point is how to determine the above three parameters with a set of experimental data. As for particle perturbation transport experiments [18], the three parameters could be determined using the different sensitivities of the phase and amplitude to these parameters. Compared with the particle transport, the problem is more complex for the heat transport since the damping time should be taken into account, while this parameter is not involved in particle transport where the loss is negligible in the core of the plasma. Figure 10 shows the sensitivity of the amplitude and phase of electron temperature Fourier components to the three major parameters. In these figures, constant χ_e, V_e and τ profiles are assumed, and the boundary conditions at the plasma centre and edge, respectively, are assumed to be $\partial \tilde{T}_e/\partial\rho|_{\rho=0} = 0$ and $\partial \tilde{T}_e/\partial\rho|_{\rho=1} = 0$. The n_e profile is assumed to be $n_e(\rho) = 1.2(1-\rho^2)^{0.5} + 0.3$; the ECRH power profile is assumed to be Gaussian in space centred at $\rho = 0.5$ with a width of $w = 5$ cm at the half height, and $P_{ecrh} = 0.5$ MW. The EC power has a square waveform with $f_{mod} = 1$ Hz and a duty factor of 0.5 in time. From figures 10(*b*), (*d*) and (*f*), we can see that the phase gradient is mainly sensitive to the diffusivity χ_e, but much less sensitive to the convection velocity V_e and the damping time τ. Specifically, the phase gradient (in absolute value) decreases when the diffusion coefficient increases and vice versa. In slab geometry, the diffusivity is simply inversely proportional to the square of the gradient of the phase [19]. Unlike the phase, the amplitude is highly sensitive to the convection velocity. For small values of V_e, only the slope of the amplitude profile is changed, while the point of the maximum of the amplitude is always located at the source position. However, for large values of V_e, the position of the maximum of the amplitude moves from the source position. If V_e is positive (inward or pinch), the maximum is shifted towards the plasma centre, if V_e is negative (outward), the maximum is shifted towards the plasma edge. As for

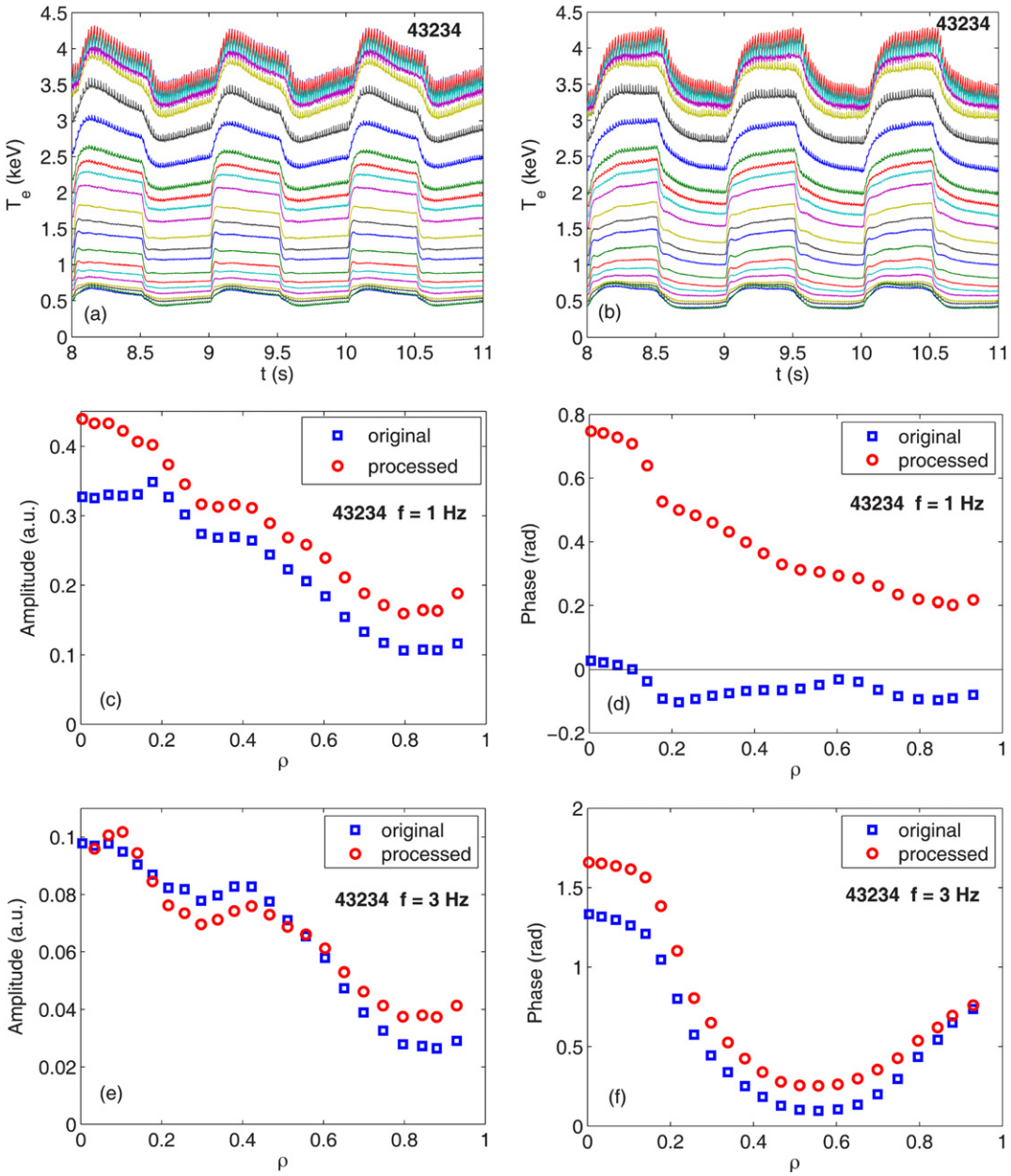

Figure 16. (*a*) shows the temperature evolution curves at different radii, and (*b*) is the modified version of T_e after correction of the density modulation effect. The amplitude and phase profiles for the first and third harmonics are shown in (*c*)–(*f*) respectively, showing the different extent of influence from density correction (shot 43234).

the damping time τ, it has opposite effects on the phase and amplitude slopes, and its impact is illustrated in figure 10. The effect of the edge boundary condition is shown in figure 11, where amplitude and phase of the first harmonics are compared for $\tilde{T}_e|_{\rho=1} = 0$ and $\partial\tilde{T}_e/\partial\rho|_{\rho=1} = 0$. It appears that the region inside the ECRH deposition is hardly affected and that the effect of the edge boundary condition decreases for increasing harmonic number. More generally, using different harmonics improves the determination of the three transport parameters by best fit or trial-and-error procedures.

The description above is just a simplified one, where the transport coefficients are assumed to be constant in radius. Since both the diffusivity and convection velocity have profiles, the real behaviour is generally more complex. In practice, when the phase or the amplitude present obvious changes in their gradients, we choose corresponding areas relative to this feature, and assume that inside each area the transport coefficients vary little. By this treatment, the LPM can be applied to the whole region.

4.3. Simulation for high density

Low-frequency modulation of ECRH at 1 Hz provides accurate measurements of the plasma response at several harmonics. For purely square-modulated wave and a duty factor of 50%, the even harmonics are absent, as seen in the experimental data where the odd harmonics are dominant. At first the signal quality in the frequency domain is qualified by the

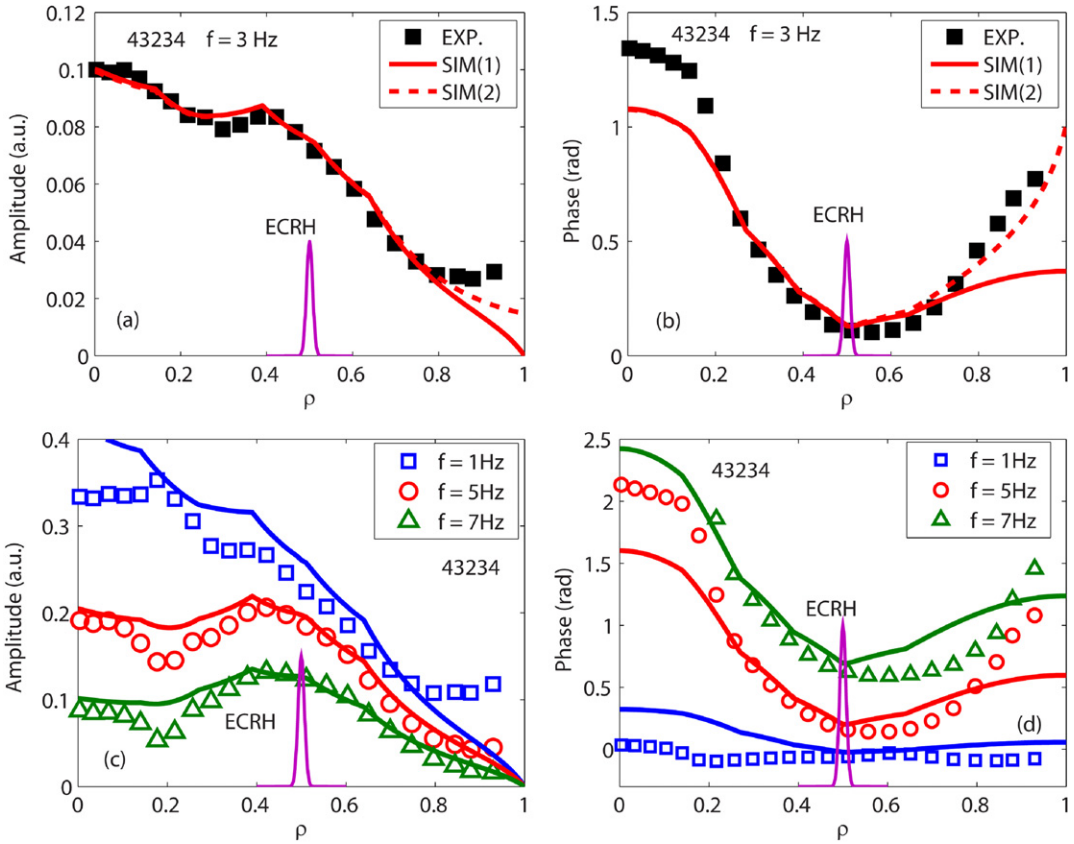

Figure 17. Simulation using the LPM for low density (TS#43234). The discrete points are experimental values, the solid lines marked by SIM(1) represent the simulation with fixed boundary condition ($\tilde{T}_{\mathrm{e\,edge}} = \mathrm{const.}$), and the dashed lines marked by SIM(2) represent the simulation with time varying edge temperature as boundary condition. Amplitude (*a*) and phase (*b*) of the third harmonic. Amplitude (*c*) and phase (*d*) of the first, fifth and seventh harmonics.

signal-to-noise ratio. In the power spectrum, the signal-to-noise ratio of each ECE channel is defined as the value of the peak divided by the mean value of the shoulders [6]. In figure 12, the signal-to-noise ratio for different harmonics for shots TS#40504 and TS#43234 is shown. Note that in the region $\rho \geqslant 0.2$, the value is higher than 5 (a reasonable limit for good detection) for harmonics from 1 to 7. However, the density oscillation may couple to the temperature oscillation, i.e. the amplitude and phase profiles of the temperature may contain the contribution from density oscillation. Due to the pure ECRH heating, the density oscillation should be a by-product compared with temperature variation. The variation of n_{e} should be slower than the T_{e}, so that the main component of n_{e} is associated with the fundamental harmonic, rather than to the higher ones. In the case of stronger n_{e} oscillations, we use higher harmonics instead; while for weaker n_{e} oscillations, we use lower harmonics, because of their higher signal-to-noise ratio.

The simulations are carried out in the whole region of plasmas. The boundary condition is set to be $\partial \tilde{T}_{\mathrm{e}}/\partial\rho|_{\rho=0} = 0$ and $\tilde{T}_{\mathrm{e}}|_{\rho=1} = \tilde{T}_{\mathrm{e\,edge}}(t)$, where the edge temperature $\tilde{T}_{\mathrm{e\,edge}}$ is taken from extrapolation of the experimental ECE data combined with Thomson scattering data.

Figure 13 shows the results of simulation with the LPM in the high-density regime (TS#40504): amplitude and phase determined from Fourier transform for the various harmonics. The transport coefficients of this simulation are shown in figure 14, as well as the effective electron heat diffusivity calculated with CRONOS. To improve the simulation, an iterative method is used in which $\chi_{\mathrm{e}} = 1\,\mathrm{m^2\,s^{-1}}$, $V_{\mathrm{e}} = 0\,\mathrm{m\,s^{-1}}$ and $\tau = 0.2\,\mathrm{s}$ are taken as initial values for shot 40504. The ion temperature is assumed to be equal to the electron temperature in the ohmic phase. For the first harmonic, the fit is good for both amplitude and phase in the whole region; for higher harmonics (third, fifth, seventh), the results of the simulation are also rather good. From figure 14(*a*), we can see that on the one hand, the heat diffusivity obtained with CRONOS (power balance) in the ECRH regime (red dotted line) is larger than that in the ohmic regime (green dashed line), except for the region just inside the ECRH power deposition layer ($0.4 < \rho < 0.5$). On the other hand, the transient heat diffusivity determined with the LPM (blue solid line) is slightly larger than that obtained with CRONOS. This just confirms the results previously obtained on other tokamaks for the perturbation transport analysis [20]. Note that, as extensively discussed in [19] (section 2.6), steady-state and perturbative analyses are expected to yield the same transport coefficients only in the ideal case of a diagonal transport matrix with constant coefficients. As shown in figure 14(*b*), the convection velocity is zero, except in the region $\rho < 0.25$; this means a diffusive propagation phenomenon of heat transport in the region $0.25 < \rho < 0.5$. From figures 13(*a*) and (*c*), we can also see that the amplitude inside $\rho = 0.25$ is higher than outside for the first harmonic. In the transport analysis, an

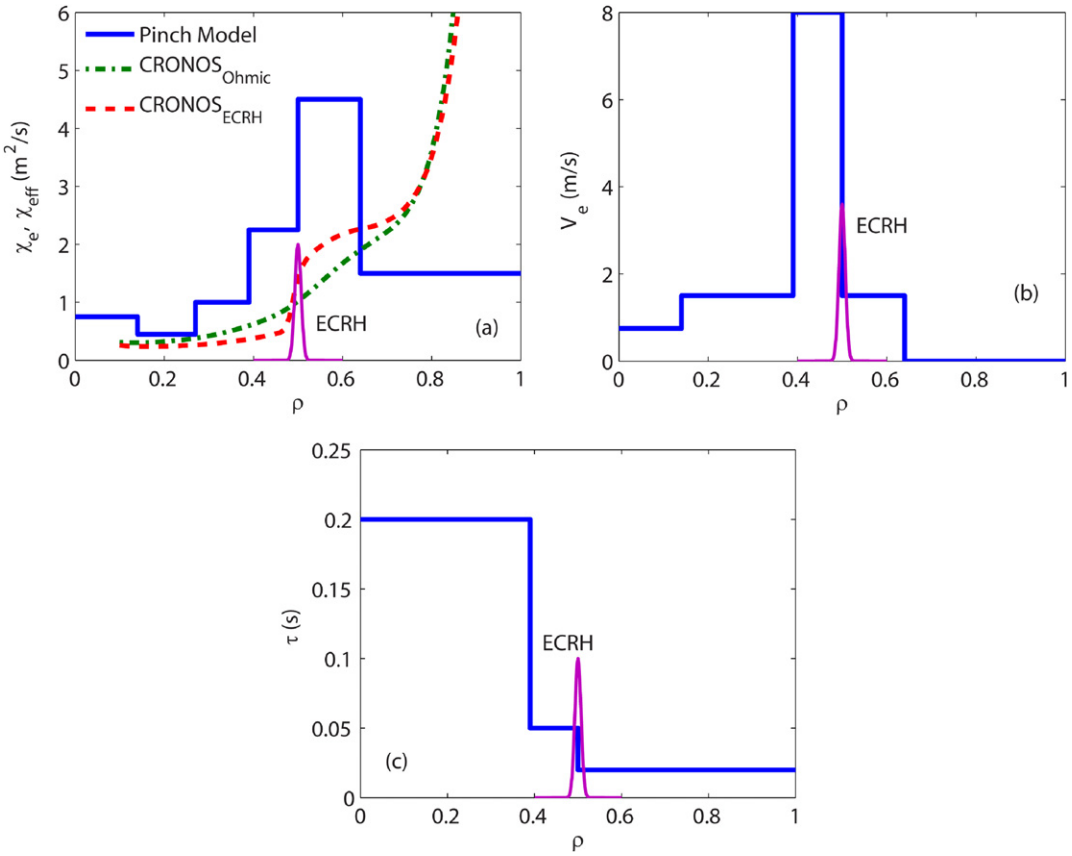

Figure 18. Parameters used for the simulation with the LPM shown in figure 16. (*a*) Diffusivity obtained by the LPM (blue solid line), by the CRONOS in the ECRH regime (red dotted line) and in the ohmic regime (green dashed line). (*b*) Pinch velocity (positive for inward convection). (*c*) Damping time.

inward convection velocity (pinch) of 3.5 m s^{-1} (figure 14(*b*)) was needed in order to reproduce the experimental points.

4.4. Simulation for low density

As mentioned in section 3.2, the temperature evolution in the lower density case is much different from that in the higher density case, because of the simultaneous density oscillations. Figure 15 shows the density and electron temperature evolution for high-density and low-density cases. It appears that in the high-density case the density varies little during the EC heating pulse, whereas in the low-density case a clear density response to the heating pulse can be identified, especially in the region $\rho < 0.8$. A simple way to correct for this effect is to multiply $T_e(r, t)$ by $n_e(r, t)/\langle n_e(r)\rangle_t$, where $\langle n_e(r)\rangle_t$ is a time average. In this way, we can get approximate temperature evolution curves, as shown in figure 16(*b*), which shows 'normal' behaviours as seen in the high-density case; the original data are also shown in figure 16(*a*).

The corresponding influence on the amplitude and phase profile for the first and third harmonics is shown in figures 16(*c*)–(*f*), from which we could draw a conclusion that the density oscillation has a stronger influence on the fundamental amplitude and phase profiles than on those of the third harmonic. In the following simulation, the third harmonic is used to determine the best fit for the transport coefficients; however, the corrected first harmonic data could also be used with similar results.

The results of the simulation for the third harmonic using the LPM are shown in figures 17(*a*) and (*b*). The experimental data are marked with discrete squares, and the solid curves are fits using the LPM with boundary condition of constant edge temperature, while the dashed curves are fits with time-varying edge temperature boundary condition. From these figures, we could find that rather good agreement to the experimental data is found for $\rho < 0.8$. In the region $\rho > 0.8$, the two boundary conditions yield different result, and the time-varying boundary condition is always in better agreement, in particular for the phase. For the purpose of clarity, only the simulation results with constant edge temperature are then shown in figures 17(*c*) and (*d*) for the first, fifth and seventh harmonics. The results of simulation for higher harmonics (fifth, seventh) are also acceptable, while for the first harmonic amplitudes show qualitative agreement and the phases are quite different, due to density effect as expected. The corresponding transport parameters in this simulation are shown in figure 18.

As expected, a large pinch velocity over a broad area ($0 < \rho < 0.7$) has been found with the LPM. This pinch velocity can reach values of order of 8 m s^{-1} near the ECRH power deposition region. This large heat pinch velocity is essential to reproduce the inward shift of the maximum of the amplitude. Now the transient heat diffusivity determined with the LPM (blue solid line) is much larger (2 or 3 times) than that obtained with CRONOS. This dependence in density of the

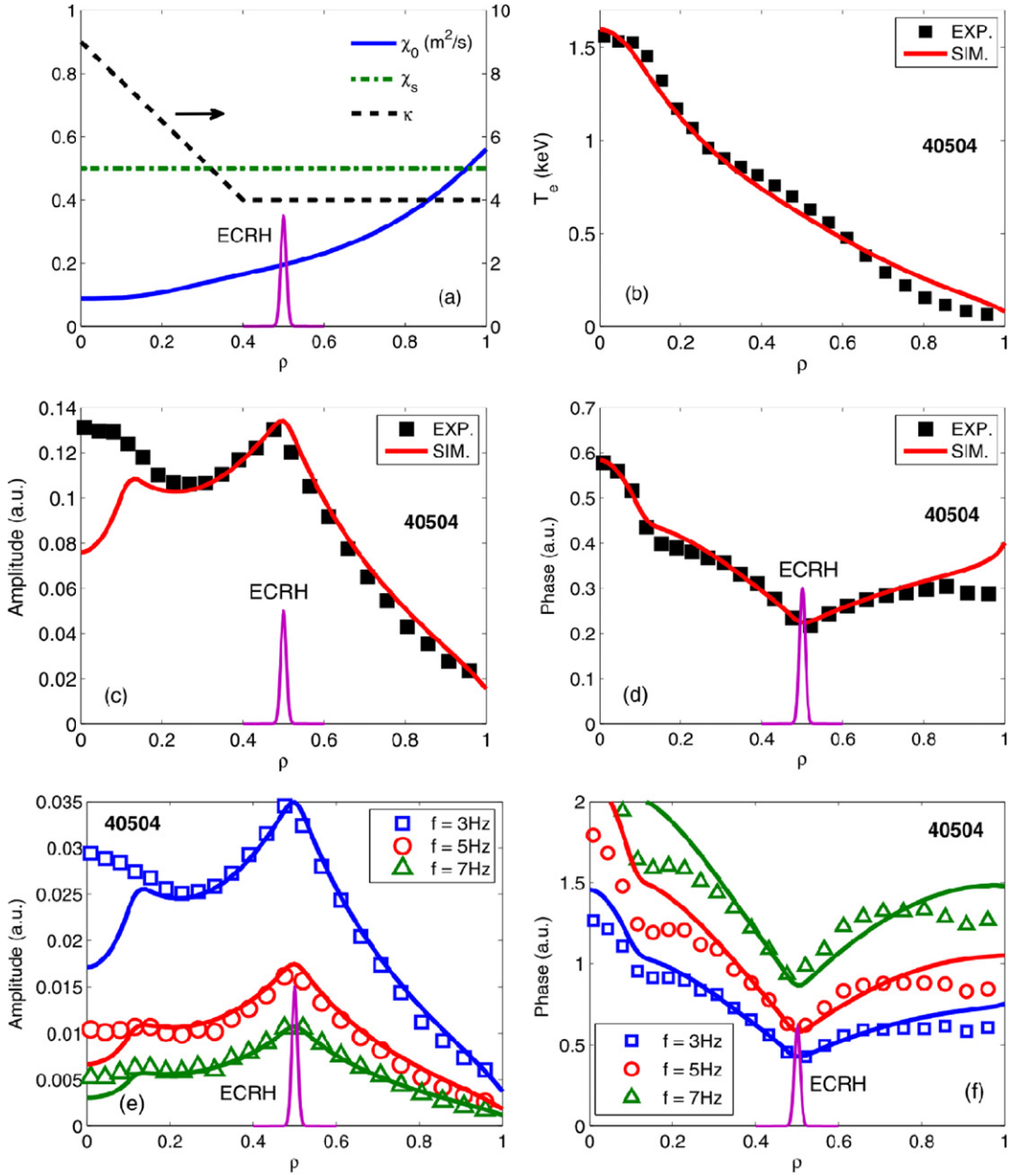

Figure 19. Simulation for shot TS#40504 using the purely diffusive CGM (with $v = 3/2$). (*a*) Parameters used in the CGM. (*b*) Electron temperature profile. (*c*) Amplitude and (*d*) phase of the fundamental harmonic. (*e*) Amplitude and (*f*) phase of the third, fifth and seventh harmonic. For (*b*)–(*f*), the discrete points represent the experimental data, and the solid curves represent the simulation results.

ratio between the transient diffusivity and that of steady state confirms the observations of ASDEX Upgrade and the related interpretation work [20]. In [20], the decrease in this ratio, when the density increases, has been interpreted as a transition from the turbulence driven by trapped electron modes (TEMs) to that driven by the ion temperature gradient (ITG) via the change in collisionality.

In summary, this modelling exercise has shown that reproducing the behaviour of several harmonics without an inward pinch would be difficult, in particular in the low-density case. The question whether a non-linear diffusive transport model could perform better to this end will be addressed in the next section.

5. Simulation using the CGM

It is commonly accepted that turbulence contributes to the main part of electron heat transport. Turbulent transport is generally induced by the growth of instabilities, in which two kinds of electrostatic drift-wave instabilities ITG and TEMs are considered to be the most likely causes of electron heat transport for low-β regimes [20], where $\beta = p/(B^2/2\mu_0)$, p is the pressure and B the magnetic field. The micro-instability analysis shows that both turbulence mechanisms have thresholds, above which the instability level is enhanced, leading to the increase in diffusivity. An empirical formula for the heat diffusivity based on the critical temperature gradient

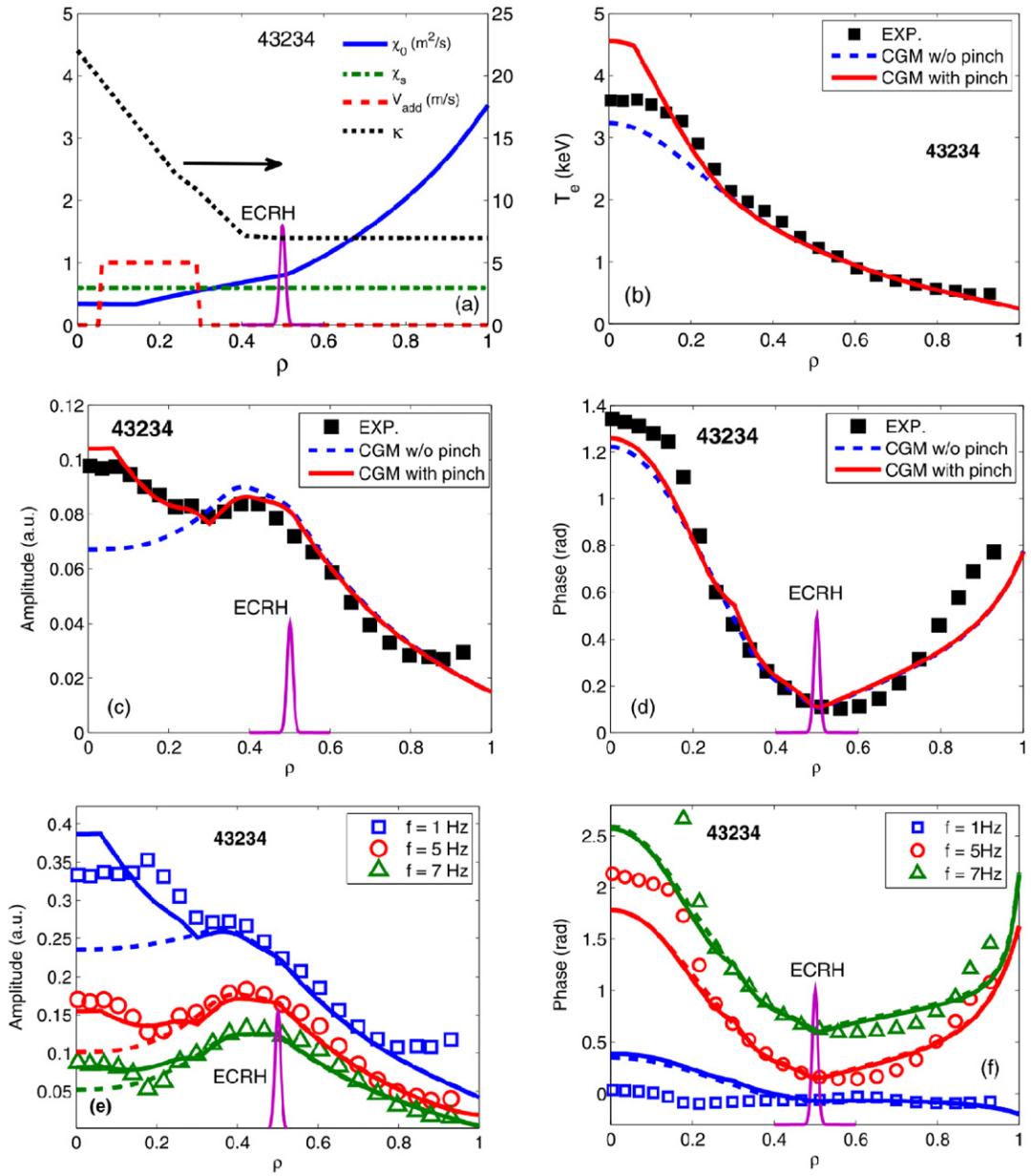

Figure 20. Simulation for shot TS#43234 using the purely diffusive CGM (with $\nu = 3/2$) and with an additional pinch term. (*a*) Parameters used in the CGM, (*b*) Electron temperature profiles in the ohmic phase. (*c*) Amplitude and (*d*) phase of the third harmonic. (*e*) Amplitude and (*f*) phase of the first, fifth and seventh harmonics. In these figures, the solid lines are simulations with pinch term, while the dashed lines are simulations without pinch.

model (CGM) has been derived (in different versions) in [6, 21]. Here we use the version of [5, 22]:

$$\chi_e = \chi_{gB}\chi_s\left(-\frac{R\partial_r T}{T} - \kappa\right) H\left(-\frac{R\partial_r T}{T} - \kappa\right) + \chi_0 \quad (3)$$

where $\chi_{gB} = q^{\nu}(T_e/eB)\rho_s/R$. Here κ is the threshold, H is the Heaviside function, χ_0 is the residual diffusivity which is responsible for heat transport whenever the inverse of the normalized temperature gradient $-R\partial_r T_e/T_e$ is lower than κ, χ_s is a stiffness factor which characterizes the strength of the critical gradient transition. In the following, $\nu = 3/2$ is chosen, as suggested in [21]. In this study, the CGM is used as a paradigm of critical temperature based models, independently of any considerations on the turbulence regime that effectively governs these discharges, and that in any case is difficult to determine with precision.

Best fit CGM parameters for the experimental data of the high-density case (shot 40504) are shown in figure 19. The ion temperature profile is simulated by means of the CRONOS code, using constraints by measurements whenever available. Sensitivity to the ion temperature profile has been found to be little. The boundary condition is assumed to be the time-varying temperature which derives from extrapolation of experimental measurements (ECE and Thomson scattering). The temperature, amplitude and phase profiles agree well with experimental data. For the fundamental and third harmonic, the amplitudes inside $\rho = 0.1$ are very low compared with experimental ones, owing to the fact that the temperature

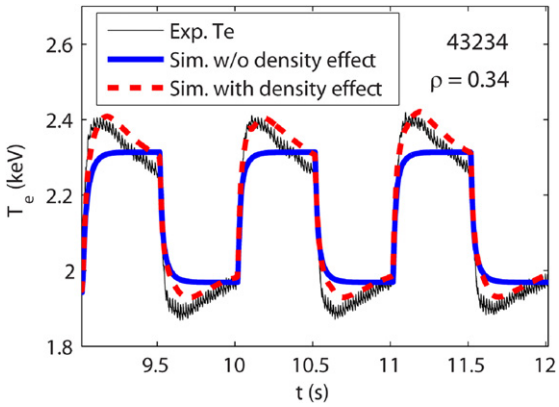

Figure 21. Comparison between the experimental data and the simulation with and without the consideration of density oscillation effect (at $\rho = 0.34$).

gradient inevitably goes below the threshold close to the plasma centre. This probably indicates that a little inward pinch could improve the agreement here; however, such a term would make the agreement on the phase worse. Note that in the LPM analysis a pinch had been added for $0.1 < \rho < 0.25$ in order to simulate this feature.

For the discharge showing an inward heat transport trend, i.e. shot 43234, the simulations with the CGM have also been performed trying to reproduce the experimental data. The best simulation is shown in figure 20, in which $\nu = 1.5$ (constant value) and the threshold value κ increases towards the centre. The main parameters used in the simulation are shown in figure 20(*a*), and in figures 20(*b*)–(*f*), the dashed curves are simulations without pinch term, and the solid curves are simulations with an additional pinch term, which is not present in the CGM. As seen in figure 20(*c*), the amplitude is lower than the experimental data in the absence of the pinch term. This suggests the necessity of adding a heat pinch to the CGM coefficients. Using a simple constant value for the pinch velocity inside $\rho < 0.3$, much better agreement on both amplitude and phase could be reached; this could of course be optimized by finely tuning the shapes of all the transport coefficients used in this simulation. Note that there is a delicate interplay between the effect of this additional pinch and the non-linearity of the CGM, in particular close to the threshold, since the heat convection modifies the temperature gradient. A more comprehensive non-linear model including heat convection should be developed for this type of comparisons.

The simulations using the CGM can be used to illustrate the role of the density variations during the ECRH modulations. To this end, the temperature evolution at $\rho = 0.34$ with time varying density profile is shown in figure 21, where other parameters are those used in the simulation with pinch term of figure 20. The four phases of the temperature evolution are well reproduced by the simulation, when the density variation is included.

The empirical CGM has been used in order to explain both the steady state and perturbation properties of the modulated discharges. The resulting heat-pulse diffusivity χ^{HP} can be written in the form of

$$\chi^{\mathrm{HP}} = \chi_{\mathrm{gB}}\chi_{\mathrm{s}}\left(-2\frac{R\partial_r T}{T} - \kappa\right) H\left(-\frac{R\partial_r T}{T} - \kappa\right) + \chi_0. \quad (4)$$

This quantity is compared with the one we used in the LPM in figure 22(*a*). In this figure, the diffusivities in ECRH and ohmic phases of the CGM and CRONOS simulations are shown. The χ^{HP} term exhibits qualitative agreement with the LPM in the region $\rho < 0.6$.

Finally, it should be stressed that inward convection is a property of the CGM, even without adding any extra pinch term. In fact, from equation (3), the effective convection velocity can be expressed by [6, 21]

$$V_{\mathrm{eff}} = \frac{1}{2}\frac{\partial_r T}{T}\chi_{\mathrm{gB}}\chi_{\mathrm{s}}\left(-\frac{R\partial_r T}{T} - 3\kappa\right) H\left(-\frac{R\partial_r T}{T} - \kappa\right) \quad (5)$$

in which $V_{\mathrm{eff}} > 0$ corresponds to an inward velocity. In this equation, for peaked profile (i.e. $\partial_r T_{\mathrm{e}} < 0$), the contribution from the gradient difference is positive when $-R\partial_r T_{\mathrm{e}}/T_{\mathrm{e}} < 3\kappa$. In our simulation, in the region $\rho < 0.3$, the normalized gradient is below the threshold, which leads to a constant diffusivity, and hence makes the effective pinch effect to vanish. The effective pinch is compared with the LPM results in figure 22(*b*).

In summary, the inward heat transport features observed in Tore Supra in low-density regimes with off-axis-ECRH modulation are likely due to the combination of two effects: a large pseudo-pinch due to the non-linearity in the heat diffusivity in the region $0.3 < \rho < 0.5$ (close to the ECRH power deposition), and a non-diffusive heat pinch in the region $\rho < 0.3$. The added pinch term has been determined by a trial-and-error procedure.

6. Conclusions

Low-frequency (1 Hz) ECRH modulation experiments have been carried out on the Tore Supra tokamak. These experiments show features that could correspond to inward heat transport, in particular in low-density discharges. Two transport models, i.e. a simple diffusive/convective model with piecewise constant coefficients (LPM) and a diffusive non-linear model (CGM), which includes a pseudo-convective term due to the temperature dependence of the diffusivity, have been applied in order to analyse the experimental behaviour. Good agreement has been found for all harmonics between the experimental data and the simulation using the LPM, which includes time constant diffusivity and convection velocity profiles. It should be emphasized that the heat diffusivity, the heat convection velocity and the damping time can be independently determined in the LPM using the sensitivity of the phase and amplitude of the modulated electron temperature relative to these three parameters. Conversely, using the purely diffusive CGM, good agreement has not been achieved: when the simulation is good for amplitude profile, the phase profile does not agree with the experimental data, and vice versa. Adding to the CGM a true heat pinch term $\sim 1\,\mathrm{m\,s^{-1}}$ inside $\rho = 0.3$ allows one to reproduce satisfactorily both experimental amplitude and phase. The magnitude of such a term has to be considered an upper limit, as we cannot exclude that different proportions of real and pseudo-pinch inside $\rho = 0.3$ could lead to equivalently good fits of the data, although such combinations have proven hard to find

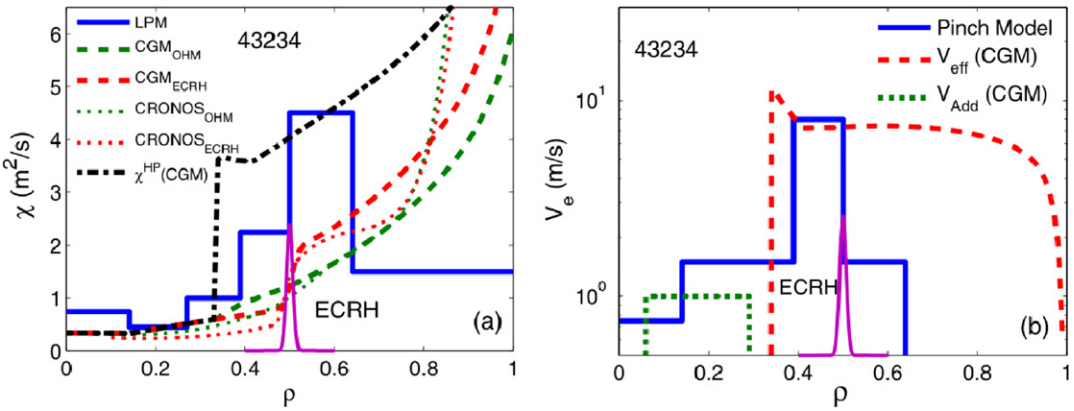

Figure 22. (*a*) Comparison of the diffusivity profiles from different models. The solid line is the diffusivity from the LPM, the thin dashed line and dotted line are ECRH and ohmic data from CRONOS simulation, and the thick dashed line and dotted line are ECRH and ohmic data from the CGM simulation. (*b*) Comparison between the value of pinch (solid line) in the LPM, effective pinch (dashed line) introduced by the CGM, and the additional pinch (dotted line) to the CGM.

in our simulations. The additional pinch plus the pseudo-pinch obtained with the CGM is roughly equivalent to the pinch obtained with the LPM. The heat-pulse diffusivity χ^{HP} resulted from the CGM is qualitatively in agreement with the diffusivity obtained with the LPM in the core ($\rho < 0.6$). It is also found that the heat pinch feature is sensitive to the plasma density, since the heat pinch tends to increase for decreasing density.

Acknowledgments

The authors acknowledge valuable discussions with F. Imbeaux, X. Garbet and G.T. Hoang. This work, supported by the European Communities under the contract of Association between EURATOM and CEA, was carried out within the framework of the European Fusion Development Agreement. The views and opinions expressed herein do not necessarily reflect those of the European Commission. Two of the authors (W.W. Xiao and B.J. Ding) were also partly supported within the framework of the cooperation between the French Commissariat à l'Energie Atomique (CEA) and, respectively, the China National Nuclear Corporation (CNNC), and the Chinese Academy of Science (CAS).

References

[1] Luce T.C., Petty C.C. and de Haas J.C.M. 1992 *Phys. Rev. Lett.* **68** 52
[2] Mantica P., Gorini G., Hogeweij G.M.D., Lopes Cardozo N.J. and Schilham A.M.R. 2000 *Phys. Rev. Lett.* **85** 4534
[3] Petty C.C. and Luce T.C. 1994 *Nucl. Fusion* **34** 121
[4] Mantica P. *et al* 2005 *Phys. Rev. Lett.* **95** 185002
[5] Mantica P. *et al* 2006 *Plasma Phys. Control. Fusion* **48** 385
[6] Imbeaux F., Ryter F. and Garbet X. 2001 *Plasma Phys. Control. Fusion* **43** 1503
[7] Lennholm M. *et al* 2003 *Nucl. Fusion* **43** 1458
[8] Krivenski V. *et al* 1985 *Nucl. Fusion* **25** 127
[9] Ségui J.L. *et al* 2005 *Rev. Sci. Instrum.* **76** 123501
[10] Gil C. *et al* 2009 *Fusion Sci. Technol.* **56** 1219
[11] Clairet F. *et al* 2001 *Rev. Sci. Instrum.* **72** 340
[12] Sabot R. *et al* 2006 *Nucl. Fusion* **46** S685
[13] Artaud J.F. *et al* 2010 *Nucl. Fusion* **50** 043001
[14] Eury S.P., Harauchamps E., Zou X.L. and Giruzzi G. 2005 *Phys. Plasmas* **12** 102511
[15] Ryter F. *et al* 2001 *Phys. Rev. Lett.* **86** 2325
[16] Zou X.L. *et al* 2003 *Nucl. Fusion* **43** 1411
[17] Clemençon A., Guivarch C., Eury S.P., Zou X.L. and Giruzzi G. 2004 *Phys. Plasmas* **11** 4998
[18] Xiao W.W. *et al*. 2010 *Rev. Sci. Instrum.* **81** 013506
[19] Lopes Cardozo N. 1995 *Plasma Phys. Control. Fusion* **37** 799
[20] Ryter F. *et al* 2005 *Phys. Rev. Lett.* **95** 085001
[21] Garbet X. *et al* 2004 *Plasma Phys. Control. Fusion* **46** 1351
[22] Casati A.*et al* 2007 *Phys. Plasmas* **14** 092303